ROYAL SOCIETY OF CHEMISTRY

PAPER

Check for updates

Investigation of the photocatalytic activity of magnetically recoverable g-C$_3$N$_4$/CoFe$_2$O$_4$/Bi$_2$MoO$_6$ particles for purifying tetracycline antibiotics: synthesis, characterization, ecotoxicity analysis, and plant toxicity test†

Zhiwei Tang, [ID] [a] Changchao Hu,*[a] Rui Zhang,*[b] Junrong Yu,[b] Lu Cai,[b] Ze Yang,[b] Xingwang Wang,[a] Shiqiang Wu[a] and Desheng Liu[a]

To purify water polluted by tetracycline antibiotics, a new visible light-driven magnetically recoverable photocatalyst, g-C$_3$N$_4$/CoFe$_2$O$_4$/Bi$_2$MoO$_6$, was prepared in this study, and it effectively removed tetracycline antibiotics. Its rapid recycling was achieved by external magnets, which greatly increased material utilization. After four repeated uses, the degradation rate of tetracycline antibiotics by the g-C$_3$N$_4$/CoFe$_2$O$_4$/Bi$_2$MoO$_6$ composite photocatalyst remained at a high level, and the magnetic separation performance remained stable. Subsequently, it was further discovered that the degradation mechanism of this photocatalytic system was consistent with a double Z-type mechanism, which enabled two transport channels for photogenerated electrons, and was favorable for the separation of the photogenerated electron–hole pairs and prolonged the lifetime of the photogenerated carriers. The active substances playing an important role in the photocatalytic system were ˙O$_2^-$ and h$^+$. In addition, the possible intermediates in the photocatalytic process were detected by GC-MS analysis, and a degradation mechanism was proposed. The ecotoxicity of the degradation products and intermediates was evaluated using the Toxicity Estimation Software Tool (TEST), and the mung bean seed cultivation test was carried out to visually and efficiently illustrate that the g-C$_3$N$_4$/CoFe$_2$O$_4$/Bi$_2$MoO$_6$ photocatalyst can effectively degrade antibiotics, with low ecotoxicity of the degradation products. This provides a new idea for the removal of organic pollutants using light energy.

1 Introduction

Tetracycline (TC) antibiotics are anti-inflammatory and immunosuppressive, and they prevent diseases or improve the growth efficiency of animals.[1–3] However, their presence in water is of concern due to their carcinogenic and toxic effects on the environment.[4–7] Chlortetracycline (CTC) is used worldwide in the livestock industry due to its low cost and high efficiency.[8–11] In contrast, the water solubility of tetracycline hydrochloride (TCH) is much higher. TCH is an antibiotic that is not easily degraded, and it can remain stable in an aqueous environment for a long time.[12–14] Because the naphthol ring in the tetracycline structure cannot be fully metabolized by organisms, more than 85% of the tetracycline is in turn excreted and accumulates in the ecological environment.[15,16] Tetracyclines have been detected in the feces of various animals at levels ranging from low μg kg^{-1} quantities up to as high as g kg^{-1}.[17,18] Therefore, there is an urgent need to remove broad-spectrum antibiotics from aqueous solutions so that such techniques can be applied to environmental waterways.

Photocatalysis is one of the most promising methods for the degradation of antibiotic contaminants due to its low cost, high efficiency, mild reaction conditions, and non-toxicity.[19,20] Since most antibiotics are resistant to decomposition due to their strong molecular structure, there is an urgent need to develop, design, and prepare suitable appropriate photocatalysts with longer wavelength absorption for the photocatalytic degradation of antibiotics.

In recent years, the advantages of bismuth-based photocatalysts have become apparent due to their strong adsorption capacity and low cost.[21] Most previous studies have focused on photocatalytic hydrogen production, water oxidation, and dye degradation, and there is a lack of research data on the degradation of antibiotics. Lone pair distortion of Bi 6 s orbitals in bismuth-based composite oxides may lead to the

[a]SINOPEC Exploration and Production Research Institute, Beijing 100083, China. E-mail: hucc2049@163.com

[b]College of Chemistry and Chemical Engineering, Southwest Petroleum University, Chengdu 610500, Sichuan, China. E-mail: zhangrui@swpu.edu.cn

overlap of O 2p orbitals and Bi 6s orbitals in the valence band, which is beneficial for reducing the band gap and photogenerated charge mobility and improving the visible light response performance.[22]

Bi_2MoO_6 is composed of alternating chalcogenide $(MoO_4)^{2-}$ and $[Bi_2O_2]^{2+}$, and therefore possesses a modifiable morphology and a suitable E_g (2.4–2.8 eV).[23] Unfortunately, the limited photoresponse range of single Bi_2MoO_6 and the limitation of its own carrier transport efficiency and transport channels lead to its poor catalytic efficiency and poor performance in practical applications.[24] In response to these shortcomings, a large number of controllable bismuth-based compounds can be prepared by morphology/structure modulation, heterostructure building, and elemental doping to address the photogenerated electron–hole pair quantum yield and separation rate problems present in Bi_2MoO_6.

Graphitic carbon nitride (g-C_3N_4) is a metal-free polymeric semiconductor with high thermal and chemical stability. Its narrow band gap of 2.7 eV allows it to directly absorb visible light without modification.[25–28] g-C_3N_4 exhibits high photocatalytic activity in the photodegradation of organic pollutants, CO_2 reduction, and hydrogen production from hydrolysis, due to its outstanding stability, non-toxicity, low cost, and effectiveness when irradiated with UV and visible light.[29] Also, the good dispersion properties of g-C_3N_4 improve the overall fraction of the composite.[30,31]

The recoverability of photocatalysts is an important indicator to evaluate their cost-effectiveness and feasibility for practical applications in antibiotic degradation. Cobalt ferrite with a spinel structure ($CoFe_2O_4$) is useful in the field of environmental remediation because of its narrow band gap, good chemical stability, ease of preparation, non-toxicity, and good catalytic properties.[32–34] $CoFe_2O_4$ has the advantage of high saturation magnetization intensity, and can provide an effective method to separate prepared composite photocatalysts, effectively solving the problem of difficult recovery of nanomaterials.[35]

The toxicity of degradation products of organic pollutants has become a subject of continuous in-depth research in photocatalysis, but intuitive and effective experimental methods are lacking. However, there has been a great deal of research on the use of plants for the degradation of antibiotics in the soil. Some plants, such as cabbage, green onions, and corn, can absorb TC from contaminated soil and water. In addition, the experimental data show that antibiotics exert varying degrees of influence on plant growth. Farkas *et al.* studied the phytotoxicity of chlortetracycline (CTC) antibiotics to pinto beans (*Phaseolus vulgaris*) and corn (*Zea mays*) under controlled conditions.[36,37] Their studies examined the accumulation and phytotoxicity of TC in these crops. Based on the above studies, the irrigation of hydroponic plants with photocatalytically treated sewage may become a more rapid, practical, and intuitive detection method for TC antibiotics.

In the current study, we synthesized magnetically recyclable g-C_3N_4/$CoFe_2O_4$/Bi_2MoO_6 (CFB) nanocomposites by hydrothermal and solvothermal methods. The photocatalytic degradation of carbon tetrachloride (20 mg L^{-1}) and tetracycline hydrochloride (TCH, 20 mg L^{-1}) was used to test the photocatalytic properties and stability of the composites. The possible photocatalytic mechanism of the system was analyzed and proposed by various characterization tools. The mass spectrometry analysis further suggested the possible degradation pathways and the ecotoxicity of the degradation products, and intermediates were evaluated using the Toxicity Estimation Software Tool (TEST). Further tests using mung bean seed cultivation were performed to visually and effectively illustrate the effect of the g-C_3N_4/$CoFe_2O_4$/Bi_2MoO_6 photocatalyst for the effective degradation of antibiotics with low ecotoxicity of the degradation products.

2 Materials and methods

2.1 Reagents

The reagents used were bismuth nitrate pentahydrate ($Bi(NO_3)_3 \cdot 5H_2O$), iron(III) chloride hexahydrate ($FeCl_3 \cdot 6H_2O$), cobalt(II) chloride hexahydrate ($CoCl_2 \cdot 6H_2O$), sodium hydroxide (NaOH), melamine ($C_3H_6N_6$), 30% ammonia solution ($NH_3 \cdot H_2O$), ethanol (C_2H_5OH), ethylene glycol ($(CH_2OH)_2$), sodium molybdate dihydrate ($Na_2MoO_4 \cdot 2H_2O$); deionized water was produced in the laboratory and used in all experiments.
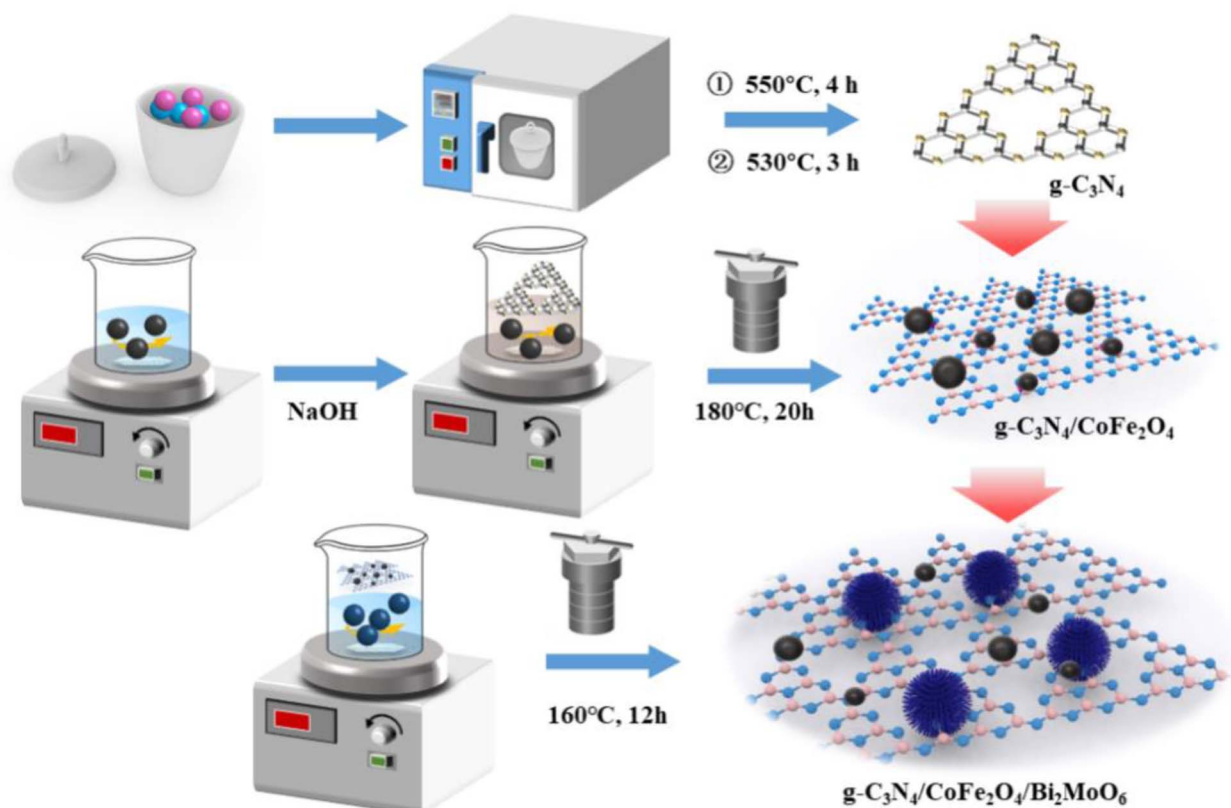
2.2 Preparation of Bi_2MoO_6 and g-C_3N_4/$CoFe_2O_4$/Bi_2MoO_6

g-C_3N_4 powder was obtained by calcining melamine twice at high temperatures, and $CoFe_2O_4$ nanoparticles were synthesized by a simple hydrothermal method. Bi_2MoO_6 was prepared by a simple solvothermal method. Briefly, $Bi(NO_3)_3 \cdot 5H_2O$ and $Na_2MoO_4 \cdot 2H_2O$ were dissolved in a mixture of $V_{(ethylene\ glycol:ethanol)} = 1:1$ by volume under magnetic stirring. The solution was stirred until it was clear and transparent, and the prepared g-C_3N_4/$CoFe_2O_4$ powder was then added under continuous stirring. The solution was transferred to a 100 mL autoclave and maintained at 160 °C for 12 hours. The final product was washed several times with absolute ethanol and dried overnight at 70 °C. In the above process, pure Bi_2MoO_6 powder was obtained without adding g-C_3N_4/$CoFe_2O_4$ powder. The process for preparation of g-C_3N_4/$CoFe_2O_4$/Bi_2MoO_6 is illustrated in Scheme 1. The detailed synthesis process is described in ESI Test S1.†

2.3 Material characterization

The crystal structure of samples was characterized using X-ray diffractometry (XRD, PANalytical B.V., X Pert PRO MPD) with Cu Kα radiation in the 2θ range of 5 to 80°. The morphology of all samples was observed by transmission electron microscopy (TEM, FEI Talos F200S). X-ray photoelectron spectroscopy (XPS) of materials was determined using a Thermo Scientific NEXSA (Al Kα radiation, XPS survey spectra: pass energy 150 eV, energy step size 1.0 eV; high-resolution XPS spectra: pass energy 50 eV, energy step size 0.05 eV) system with an Avantage data processing system. The fluorescence intensity can determine the migration and recombination of photogenerated electron–hole pairs in a semiconductor. To study the magnetic strength of the materials, the hysteresis loop of the sample was obtained

Scheme 1 Preparation process for the g-C$_3$N$_4$/CoFe$_2$O$_4$/Bi$_2$MoO$_6$ composites.

through vibrating sample magnetometry (VSM, LakeShore 7404) test, and the magnetic field range was between −2 T and 2 T. N$_2$ adsorption–desorption experiments were carried out on pretreated samples under 77 K liquid nitrogen (BET, Micromeritics ASAP 2460). The specific surface area of the material was calculated by the Brunauer–Emmett–Teller (BET) equation in the range of 0.05–0.35 relative pressure, and the pore size distribution of the sample was analyzed by the Barrett–Joyner–Halenda (BJH) model. The photoluminescence (PL) spectra of samples were obtained using a fluorescence spectrophotometer (PerkinElmer LS55, USA). The UV-Vis diffuse reflectance spectroscopy (DRS) spectra of samples were investigated using a PerkinElmer Lambda 850 analyzer (Platinum Elmer Instrument Co., Ltd, USA). The electrochemical impedance spectroscopy (EIS) curve was tested using an electrochemical workstation. A Pt electrode, standard calomel electrode, and fluorine-doped tin oxide (FTO) electrode were used as the counter electrode, reference electrode, and working electrode, respectively.

2.4 Electrochemical measurements

The photoelectrochemical properties of samples were determined using an electrochemical workstation (CHI604D, CH Instruments, Inc., Shanghai, China) equipped with a standard three-electrode system. Pt was used as the counter electrode, saturated calomel was used as the reference electrode, and an

FTO glass acted as the working electrode. In addition, the electrolyte was Na$_2$SO$_4$ solution (0.5 M), and the light source was a 500 W Xe lamp.

2.5 Photocatalytic activity test

The photocatalytic activity of the sample was evaluated by degrading TC under visible light. The visible light irradiation was emitted from an incandescent lamp of 200 W, and the distance from the light source to the ultrafiltration cup was 15 cm. TC suspension was withdrawn at regular intervals during the illumination, and after centrifugation. The concentration of TC was measured at 369 nm (CTC) and 359 nm (TCH) using a UV-Vis spectrometer (UV-1800, Shimadzu, Japan). The removal efficiency of TC was calculated using the following formula: $\eta = \dfrac{C_t - C_0}{C_0} \times 100$, where C_0 denotes the initial concentration of TC, and C_t denotes the concentration of TC when the reaction time was t.

2.6 Radical-capturing experiment

A radical-capturing experiment is an effective means to explain the reaction mechanism. Radical capturing agents were added during photocatalytic testing. Isopropanol (IPA, 10 mmol L^{-1}), ethylenediaminetetraacetic acid disodium salt (EDTA-2Na, 10 mmol L^{-1}), benzoquinone (BQ, 1 mmol L^{-1}), and methanol (MeOH, 10 mmol L^{-1}) were added as scavengers for

hydroxyl radicals (˙OH), photo-generated holes (h⁺), superoxide radicals (˙O$_2^-$), and sulfate radicals (˙SO$_4^-$).

2.7 Toxicity assessment

Toxicity assessment is of great interest in evaluating the safety of wastewater treatment processes because of the potential formation of highly toxic intermediates during degradation.[38] The potential toxicity of AMP and identified intermediates were predicted based on the quantitative structure–activity relationship (QSAR) method using computerized prediction systems (ecological structure–activity relationships (ECOSAR) and Toxicity Estimation Software Tool (TEST) programs) developed by the United States Environmental Protection Agency (EPA). TEST was used to assess the ecotoxicity of CTC and its transformation products. The fathead minnow LC50 (96 h), *Daphnia magna* LC50 (48 h), oral rat LD50, bioaccumulation factor, developmental toxicity, and Ames mutagenicity were determined by the TEST analysis.

Furthermore, this work used the mung bean, which is an economically relevant dicotyledonous species of bean consumed worldwide. Germination and growth experiments were conducted in pure water, 10 mg L^{-1} CTC, 20 mg L^{-1} CTC, 50 mg L^{-1} CTC solution, and 20 mg L^{-1} CTC solution after photodegradation treatment. Detailed information on growth experiments has been described.

3 Results and discussion

3.1 Characterization of g-C$_3$N$_4$/CoFe$_2$O$_4$/Bi$_2$MoO$_6$

The crystal structures and phase purity of the prepared materials were tested by XRD, and the results are shown in Fig. 1. Pure CoFe$_2$O$_4$ and Bi$_2$MoO$_6$ correspond to JCPDS Nos. 22-1086 and 21-0102, respectively. The characteristic peaks of pure g-C$_3$N$_4$ at $2\theta =$ 13.0° and 27.6° indicate the (100) and (002) diffraction surfaces of graphite-like carbonitrides, respectively. The characteristic

diffraction peaks of the composites CoFe$_2$O$_4$/Bi$_2$MoO$_6$ and g-C$_3$N$_4$/CoFe$_2$O$_4$/Bi$_2$MoO$_6$ are generally similar in position to those of the Bi$_2$MoO$_6$ monomer, with enhanced intensity compared to that of the monomer, and showing the characteristic peaks of the CoFe$_2$O$_4$ monomer at 30.2° and 35.5°. In addition, the diffraction peak of g-C$_3$N$_4$ was not found in the ternary complex, as it disappeared due to the low content of g-C$_3$N$_4$.[39] However, the characteristic peak at 27.6° was significantly enhanced compared to the CoFe$_2$O$_4$/Bi$_2$MoO$_6$ composite.

To investigate the surface elemental composition of the composite, XPS tests were carried out. As shown in Fig. 2a, two binding energy values of 284.8 eV and 288.1 eV in the C 1s spectrum were identified as overlapping peaks of the sp^2 C–N bond and C–(N)$_3$.[40,41] The addition of CoFe$_2$O$_4$ and Bi$_2$MoO$_6$ resulted in the appearance of a new peak at 286.5 eV, corresponding to the C–O bond, which can strongly demonstrate a successful composite of g-C$_3$N$_4$ in the CFB ternary composite.[42] Furthermore, the difference in peak intensities and slight peak shifts suggest the existence of interactions between C and other elements. In the N 1s spectrum (Fig. 2b), the peaks at 398.33 eV and 400.73 eV correspond to the C–N–C structure and the C–N–H bond, respectively.[43–45]

The high-resolution XPS spectrum of O 1s is shown in Fig. 2c, with the binding energy at 530.0 eV attributed to O^{2-} in Bi$_2$MoO$_6$ and CoFe$_2$O$_4$, and the association of the peaks at 531.5 eV and 532.6 eV with the binding energy of –OH. The high resolution spectrum of Bi 4f is shown in Fig. 2d, with the peak at 158.52 eV appearing to be in agreement with the standard. The binding energy at 163.82 eV was displaced from the standard value of 162.3 eV for the spin–orbit component of Bi 4f$_{5/2}$, indicating a change in the chemical environment of Bi at this time. The two characteristic peaks in Fig. 2e with binding energies of 232.3 eV and 235.4 eV were attributed to Mo 3d$_{5/2}$ and Mo 3d$_{3/2}$, respectively, which demonstrated the presence of Mo^{6+} in the complex. The diffraction peaks with binding energies of 710.76 eV and 724.42 eV in Fig. 2f correspond to Fe 2p$_{3/2}$ and Fe 2p$_{1/2}$, respectively, and Fe 2p$_{3/2}$ and Fe 2p$_{1/2}$ satellite peaks also appear in the complex, which indicate the presence of Fe elements in the form of Fe^{3+} in the complex. In addition, the diffraction peaks at 780.8 eV and 796.2 eV in Fig. 2g correspond to Co 2p$_{3/2}$ and Co 2p$_{1/2}$, and the diffraction peaks at 786.0 eV and 802.3 eV were attributed to the Co 2p$_{3/2}$ and Co 2p$_{1/2}$ satellite peaks, respectively, thus indicating the presence of Co in the form of Co^{2+}. The above results further indicate the successful preparation of composites composed of g-C$_3$N$_4$, CoFe$_2$O$_4$, and Bi$_2$MoO$_6$.

The morphology and microstructure of the prepared photocatalysts were characterized using scanning electron microscopy (SEM) and transmission electron microscopy (TEM). The SEM images in Fig. 3c–e show that g-C$_3$N$_4$ is a stacked nanosheet, CoFe$_2$O$_4$ nanoparticles exhibit a short rod-like structure, and Bi$_2$MoO$_6$ exhibits a nano-microsphere structure. The SEM and TEM images of g-C$_3$N$_4$/CoFe$_2$O$_4$/Bi$_2$MoO$_6$ in Fig. 3f,a and b, respectively, show that the short-rod-like CoFe$_2$O$_4$ is associated with the spherical Bi$_2$MoO$_6$ and is tightly attached and uniformly deposited on the g-C$_3$N$_4$ nanosheets, which facilitates the transport of photogenerated electrons between the heterojunctions.
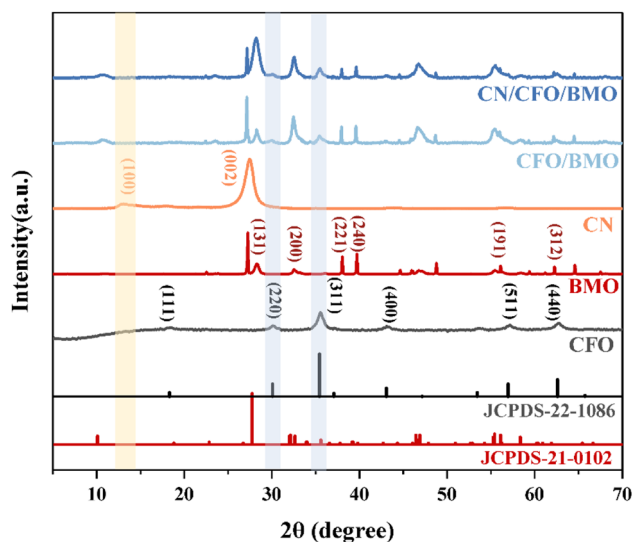

Fig. 1 XRD patterns of g-C$_3$N$_4$/CoFe$_2$O$_4$/Bi$_2$MoO$_6$, CoFe$_2$O$_4$/Bi$_2$MoO$_6$, g-C$_3$N$_4$, Bi$_2$MoO$_6$, and CoFe$_2$O$_4$.
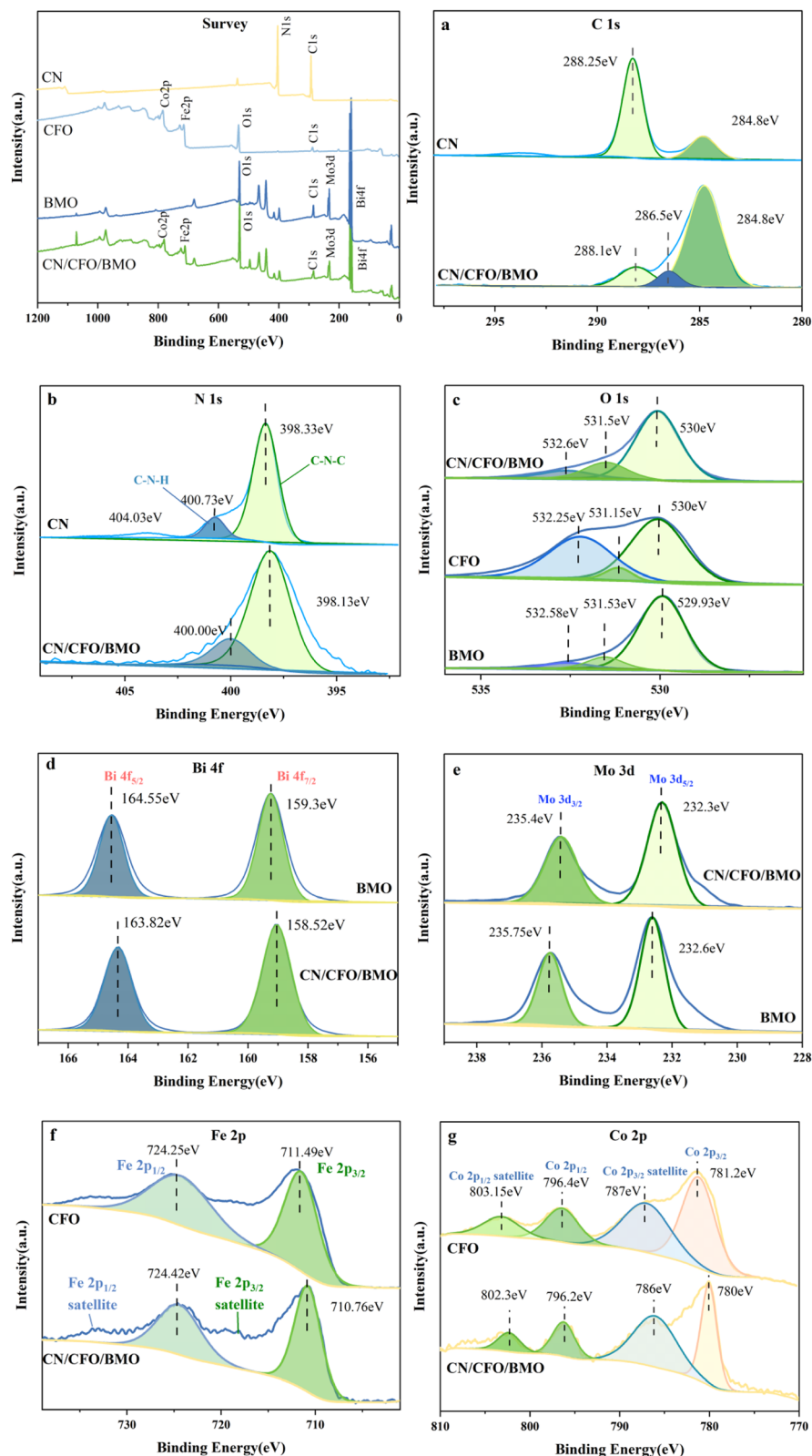
Fig. 2 XPS survey spectra, (a) C 1s, (b) N 1s, (c) O 1s, (d) Bi 4f, (e) Mo 3d, (f) Fe 2p, and (g) Co 2p.

Based on the results of theoretical and previous XRD crystal structure data, it is possible to associate transparent streaks with a spacing of 0.223 nm with the Bi_2MoO_6 (2 4 0) lattice plane, and transparent streaks with spacings of 0.289 nm and 0.436 nm with the $CoFe_2O_4$ (2 2 0 0) and (1 1 1) lattice planes, respectively. In addition, the EDS images (Fig. 3c) show that
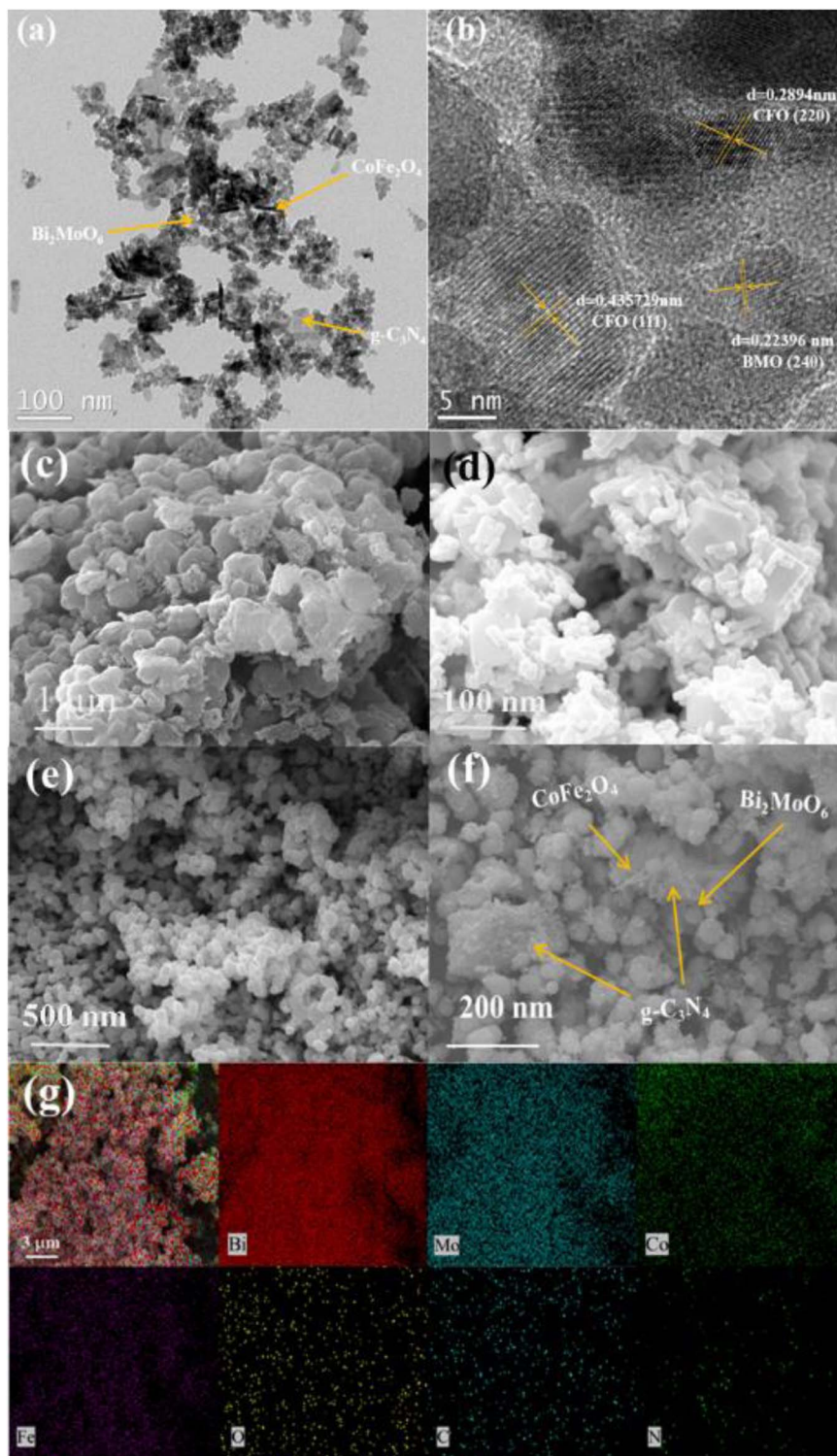
Fig. 3 TEM images of (a, b and f) g-C_3N_4/$CoFe_2O_4$/Bi_2MoO_6. SEM images of (c) g-C_3N_4, (d) $CoFe_2O_4$, and (e) Bi_2MoO_6. EDX images of (g) g-C_3N_4/$CoFe_2O_4$/Bi_2MoO_6.

the elements of Bi, Mo, Co, Fe, C, N, and O in the composites were uniformly distributed on the surface of the materials, further indicating the formation of a g-C_3N_4/$CoFe_2O_4$/Bi_2MoO_6 heterojunction photocatalyst.

The specific surface area and pore structure were tested using N_2 adsorption–desorption. The isotherms shown in Fig. 4 exhibit a typical IV curve with a small hysteresis loop, indicating that the obtained photocatalysts are mesoporous materials.
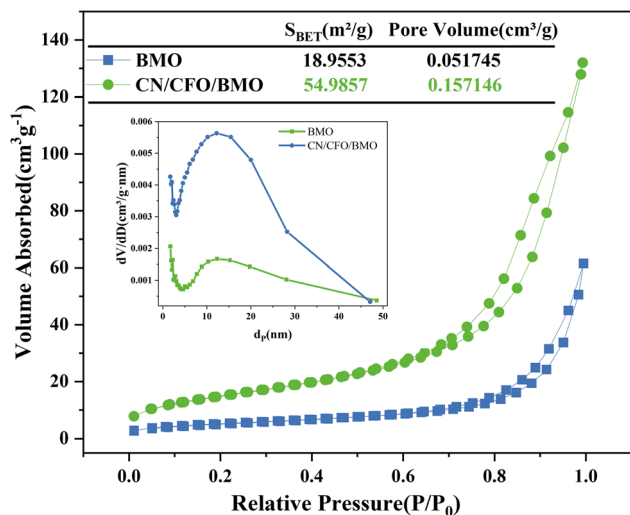
Fig. 4 Nitrogen adsorption–desorption isotherm curves and the corresponding pore size distribution for Bi_2MoO_6 and $g-C_3N_4/CoFe_2O_4/Bi_2MoO_6$.

Pore size distribution curves (inset) further confirm the existence of mesopores in the range of 2–30 nm. The specific surface area of $g-C_3N_4/CoFe_2O_4/Bi_2MoO_6$ (54.9857 m^2 g^{-1}) was calculated from the BET equation, and was found to be larger than that of Bi_2MoO_6 (18.9553 m^2 g^{-1}), with a larger average pore volume. Therefore, during the photocatalytic reaction, the $g-C_3N_4/CoFe_2O_4/Bi_2MoO_6$ complex can provide a large number of surface-active sites, which is beneficial for improving the photocatalytic activity.

Fig. 5 shows the hysteresis lines of the composite photocatalysts. The results show that there is a certain magnetic saturation intensity for all four samples, with 65.2 emu g^{-1}, 23.1 emu g^{-1}, and 18.9 emu g^{-1} for $CoFe_2O_4$, $CoFe_2O_4/Bi_2MoO_6$, and $g-C_3N_4/CoFe_2O_4/Bi_2MoO_6$, respectively. There were much lower magnetic saturation intensities for the prepared $CoFe_2O_4/$
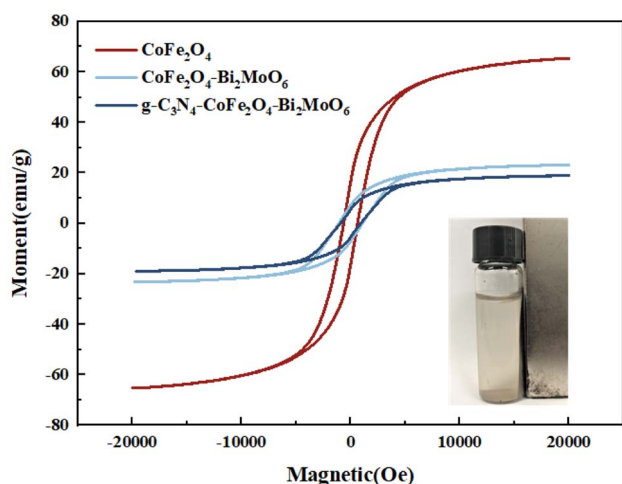

Fig. 5 VSM spectra of $g-C_3N_4/CoFe_2O_4/Bi_2MoO_6$, $CoFe_2O_4/Bi_2MoO_6$, and $CoFe_2O_4$.

Bi_2MoO_6 and $g-C_3N_4/CoFe_2O_4/Bi_2MoO_6$ composite photocatalysts as compared to the $CoFe_2O_4$ nanoparticles, which was mainly due to the change in the $CoFe_2O_4$ content caused by the addition of Bi_2MoO_6 and $g-C_3N_4$, and the modification of the non-magnetic material Bi_2MoO_6 on the surface of $CoFe_2O_4$. This result is in accordance with the XRD test, where the intensity of the characteristic peak alteration was consistent. Although the magnetic saturation intensities of the two composites were reduced compared to the monomer, they retained their magnetically separable properties.

To test the optical properties of the photocatalyst, UV-Vis DRS was used to investigate the light absorption of the prepared samples, and the results are shown in Fig. 6. The forbidden bandwidths of the semiconductor photocatalysts were further calculated, and the results are shown in Fig. 6b. As shown in Fig. 6a, for the light green Bi_2MoO_6, there is a significant amount of light absorption in the UV region and almost no absorption in the visible range, with an absorption sideband at 420 nm. $CoFe_2O_4$ shows strong absorption in the wavelength range of 200–800 nm. Compared with $CoFe_2O_4/Bi_2MoO_6$, the addition of $g-C_3N_4$, for which the maximum absorbed light wavelength is approximately 470 nm, resulted in an extension of the light absorption capacity of the ternary composites to the infrared region greater than 900 nm, and the light absorption capacity was further enhanced. This phenomenon may be attributed to the introduction of the appropriate amount of $g-C_3N_4$, which enlarges the specific surface area of the material and facilitates a stronger connection of $CoFe_2O_4$ and Bi_2MoO_6, and in turn improves the light absorption performance of the photocatalyst material.

The band gap energy of the samples can be used to further explore the photocatalytic degradation mechanism. The band gap widths of $g-C_3N_4$, $CoFe_2O_4$, and Bi_2MoO_6 can be calculated according to E_q. Because $g-C_3N_4$ and $CoFe_2O_4$ are direct leap semiconductor catalysts, $n = 1$. Bi_2MoO_6 is an indirect leap semiconductor catalyst, and therefore, $n = 4$. The Kubelka–Munk curves were calculated from empirical equations, and the bandwidths of $g-C_3N_4$, $CoFe_2O_4$, and Bi_2MoO_6 were estimated to be 2.90 eV, 1.36 eV, and 2.68 eV, respectively.

The rate of electron–hole pair transfer and complexation is the main influencing factor on the photocatalytic performance of the material. The photogenerated electron and hole complexation of the catalysts was investigated by fluorescence and impedance test experiments. Fig. 7 shows the PL spectra of pure $CoFe_2O_4$, pure Bi_2MoO_6, $CoFe_2O_4/Bi_2MoO_6$, and the $g-C_3N_4/CoFe_2O_4/Bi_2MoO_6$ composites at 320 nm excitation wavelength.

As can be seen from the figures, the PL emission peaks of all samples are in the range of 340–450 nm. Compared with pure $CoFe_2O_4$ and Bi_2MoO_6, the PL emission peak intensity of the $CoFe_2O_4/Bi_2MoO_6$ composite catalyst was significantly weaker, indicating that the formation of heterojunctions in the composite photocatalytic materials can increase the separation efficiency of photogenerated electrons and holes to a certain extent. $g-C_3N_4$ can effectively prevent photogenerated carrier compounding. The catalysts can generate additional active

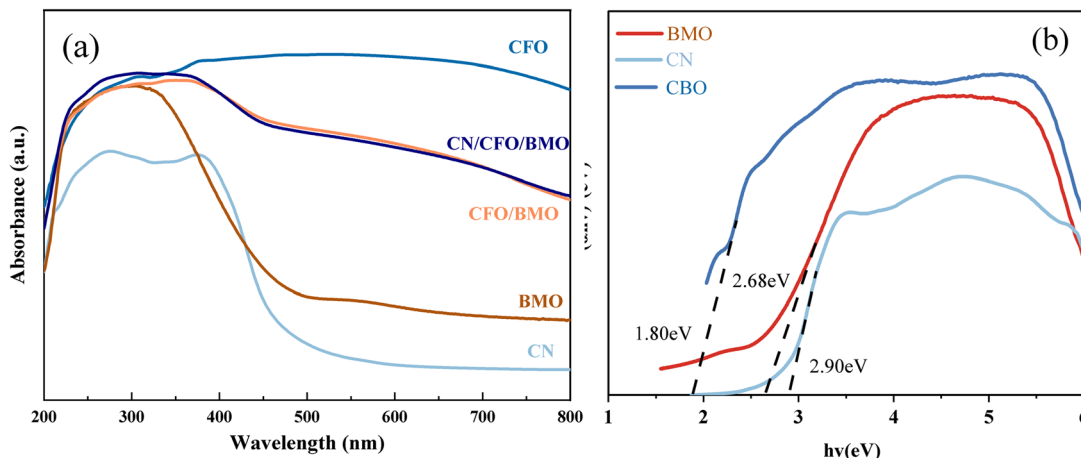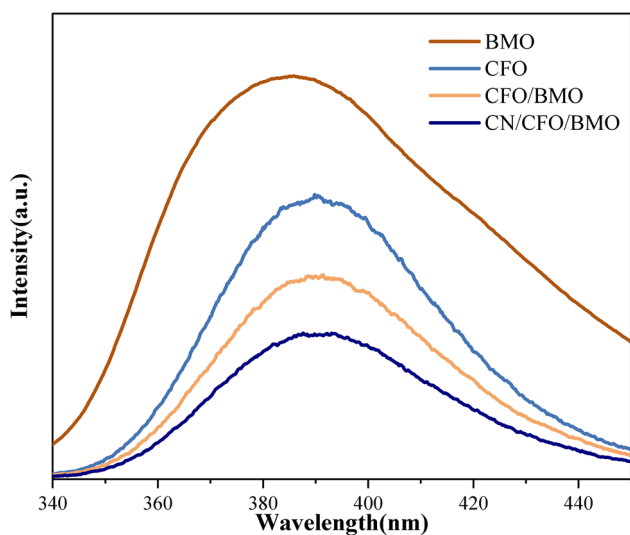**Fig. 6** UV-Vis DRS (a) spectra for all samples, and (b) a plot of $(\alpha h\nu)^2$ *vs. hν* (inset) for g-C$_3$N$_4$, CoFe$_2$O$_4$, and Bi$_2$MoO$_6$.

Fig. 7 The PL spectra of CoFe$_2$O$_4$, Bi$_2$MoO$_6$, and the CoFe$_2$O$_4$/Bi$_2$MoO$_6$, and g-C$_3$N$_4$/CoFe$_2$O$_4$/Bi$_2$MoO$_6$ composites.

Fig. 8 The EIS spectra for the g-C$_3$N$_4$, CoFe$_2$O$_4$, Bi$_2$MoO$_6$, CoFe$_2$O$_4$/Bi$_2$MoO$_6$, and g-C$_3$N$_4$/CoFe$_2$O$_4$/Bi$_2$MoO$_6$ composites.

oxide species in the photocatalytic process and enhance the photocatalytic activity of the catalysts.

3.2 Electrochemical analysis

To further investigate the electronic conduction of the prepared samples, EIS analyses were carried out for g-C$_3$N$_4$, CoFe$_2$O$_4$, Bi$_2$MoO$_6$, CoFe$_2$O$_4$/Bi$_2$MoO$_6$, and g-C$_3$N$_4$/CoFe$_2$O$_4$/Bi$_2$MoO$_6$. Fig. 8 shows that the radii of circularity are smaller for the CoFe$_2$O$_4$/Bi$_2$MoO$_6$ and g-C$_3$N$_4$/CoFe$_2$O$_4$/Bi$_2$MoO$_6$ composites, *i.e.*, lower resistance, compared to pure CoFe$_2$O$_4$ and Bi$_2$MoO$_6$, which facilitates the charge transfer between the interfaces. It was noted that the smallest radius was for g-C$_3$N$_4$/CoFe$_2$O$_4$/Bi$_2$MoO$_6$, indicating that the electron–hole pair separation was the most efficient, and the addition of g-C$_3$N$_4$ as a functional material to accelerate electron conduction is one of the factors that contributed to this efficiency. The above results are consistent with the findings of PL spectroscopy and also provide a theoretical basis for the results of the photocatalytic activity evaluation.

To better present the degradation mechanism of the g-C$_3$N$_4$/CoFe$_2$O$_4$/Bi$_2$MoO$_6$ photocatalyst, the flat-band potentials of Bi$_2$MoO$_6$, CoFe$_2$O$_4$, and g-C$_3$N$_4$ were tested using an electrochemical workstation, as shown in the Mott–Schottky (M–S) curves in Fig. 9. Once the M–S curves were obtained, the intercepts were plotted towards the horizontal axis, and the slopes of g-C$_3$N$_4$, CoFe$_2$O$_4$, and Bi$_2$MoO$_6$ were positive and were therefore identified as n-type semiconductors. The intercept results show that the flat-band potentials U_{fb} for g-C$_3$N$_4$, CoFe$_2$O$_4$, and Bi$_2$MoO$_6$ are −1.15 V (*vs.* saturated glycogen electrode (SCE), 0.27 V (*vs.* SCE), and −0.80 V (*vs.* SCE), respectively. Because the standard hydrogen electrode (NHE) = SCE + 0.24 V, the flat-band potentials of g-C$_3$N$_4$, CoFe$_2$O$_4$, and Bi$_2$MoO$_6$ are equal to −0.91 V (*vs.* NHE), 0.51 V (*vs.* NHE), and −0.56 V (*vs.* NHE), respectively. The conduction band potential of n-type semiconductors is 0.1–0.3 V lower than that of the flat band potential, and the conduction band (CB) values for g-C$_3$N$_4$, CoFe$_2$O$_4$, and Bi$_2$MoO$_6$ were estimated
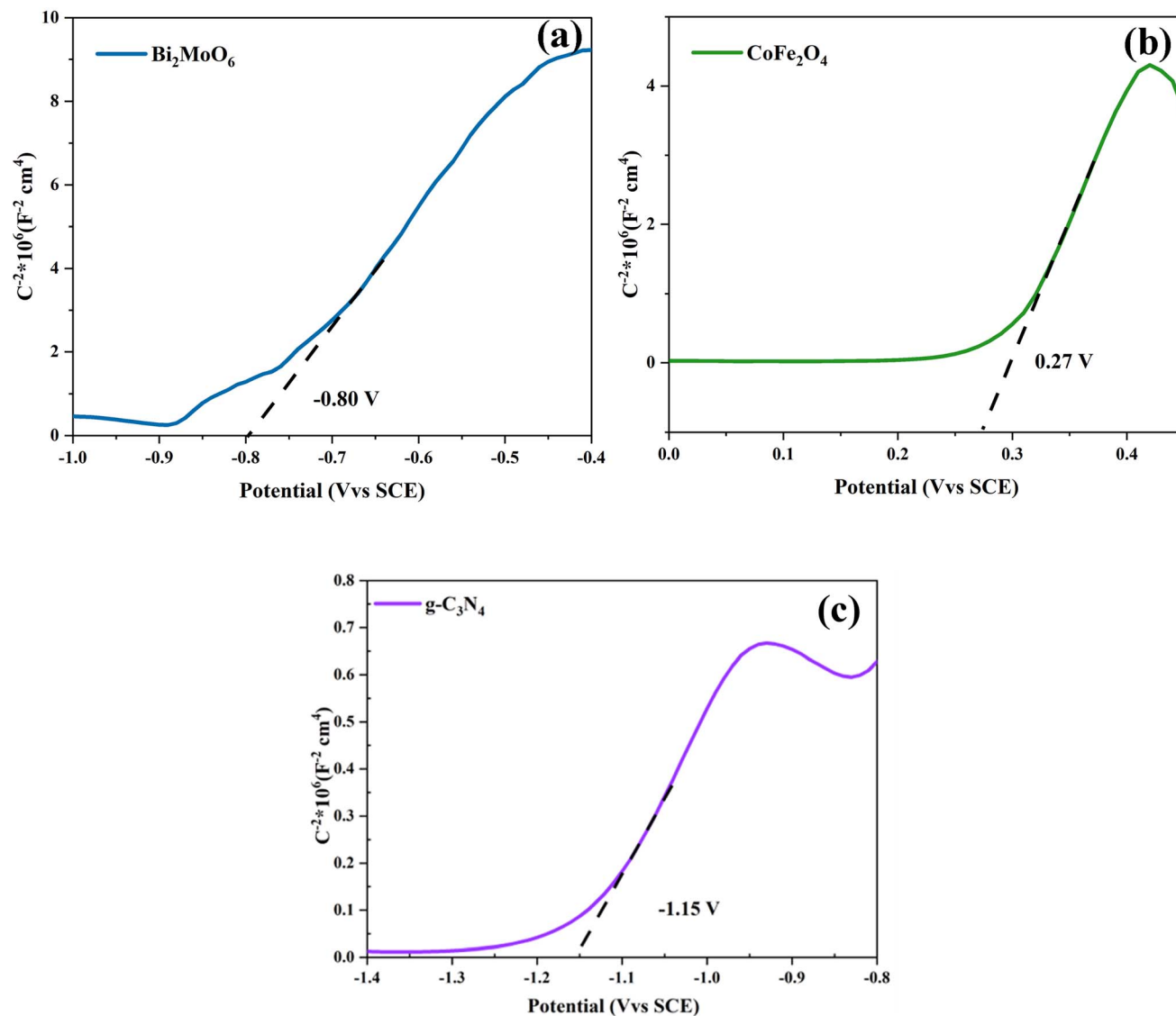
Fig. 9 Mott–Schottky plot of (a) Bi_2MoO_6, (b) $CoFe_2O_4$, and (c) g-C_3N_4.

to be -1.01 eV, 0.41 eV, and -0.66 eV (*vs.* NHE), respectively. The forbidden bandwidths of g-C_3N_4, $CoFe_2O_4$, and Bi_2MoO_6 were estimated to be 2.90 eV. The valence band (VB) values for g-C_3N_4, $CoFe_2O_4$, and Bi_2MoO_6 were estimated to be 1.89 eV, 1.77 eV, and 2.02 eV, respectively, from the equation $E_{CB} = E_{VB} - E_g$.

3.3 Photocatalytic degradation performance

The photocatalytic performance of the prepared $CoFe_2O_4$, Bi_2MoO_6, g-C_3N_4, $CoFe_2O_4/Bi_2MoO_6$, and g-$C_3N_4/CoFe_2O_4/Bi_2MoO_6$ composites was evaluated by degrading two organic pollutants: chlortetracycline (CTC, 20 mg L^{-1}) and tetracycline hydrochloride (TCH, 20 mg L^{-1}). The degradation curves of CTC on chlortetracycline hydrochloride shown in Fig. 10a indicate that the Bi_2MoO_6 monomer and g-C_3N_4 monomer are less effective in photocatalysis.

The adsorption capacity of the $CoFe_2O_4$ monomer for CTC on tetracycline hydrochloride was satisfactory, reaching 33%

adsorption efficiency within 30 min, which was attributed to the large specific surface area of the $CoFe_2O_4$ nanoparticles and the positive surface charge. The photocatalytic performance of the prepared g-$C_3N_4/CoFe_2O_4/Bi_2MoO_6$ heterojunctions was excellent, and the photocatalytic performance of the g-$C_3N_4/CoFe_2O_4/Bi_2MoO_6$ heterojunctions of various ratios was higher than that of other materials. The above phenomena mainly occurred because the formation of ternary heterojunctions promotes charge transfer and reduces the electron and hole complexation rate. The degradation curves of the photocatalyst for TCH are shown in Fig. 10b, and the degradation efficiency results were almost identical to the pattern for CTC, with the g-$C_3N_4/CoFe_2O_4/Bi_2MoO_6$ composites also exhibiting high photocatalytic activity in degrading the antibiotic TCH.

The overall photocatalytic performance of the ternary composites was more optimal than that of the binary composites after the successful introduction of g-C_3N_4. When the content was 5%, the g-$C_3N_4/CoFe_2O_4/Bi_2MoO_6$ composites
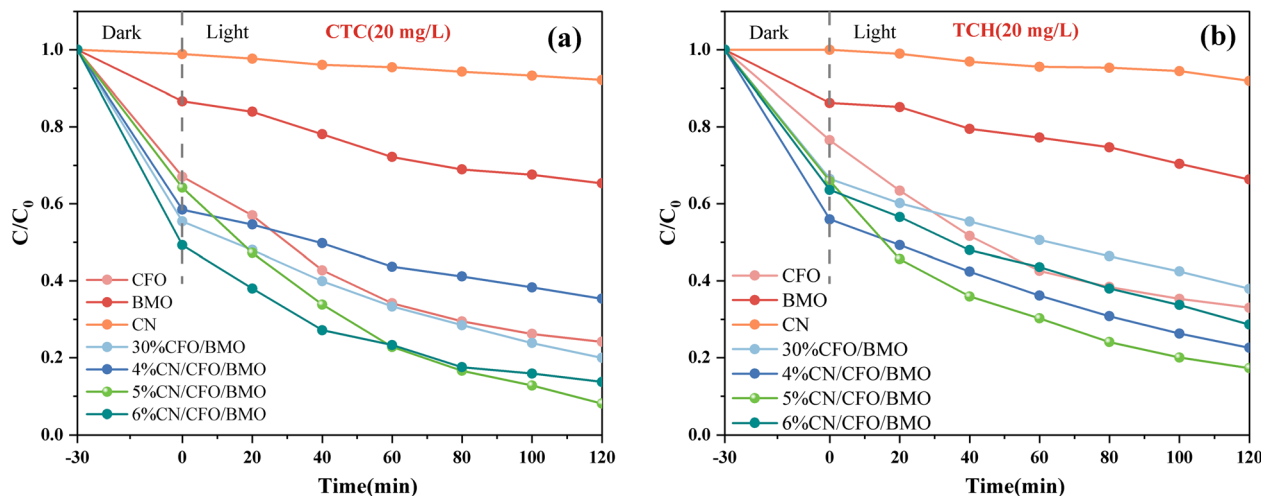
Fig. 10 The photo-degradation curves of (a) CTC and (b) TCH by the prepared photocatalyst under visible light irradiation ([photocatalyst] = 0.5 mg mL^{-1}; [pollutant] = 20 mg L^{-1}, 100 mL; initial pH = 7; temperature = 30 ± 0.5 (°C).

showed more excellent photocatalytic performance, and the strongest photocatalytic performance was for the g-C$_3$N$_4$/CoFe$_2$O$_4$/Bi$_2$MoO$_6$ composites. The degradation rates for TCH and CTC were 82.7% and 91.9% within 2 h, respectively.

In addition, the effects of the g-C$_3$N$_4$ and CoFe$_2$O$_4$ content on the photocatalytic degradation of CTC and TCH were also investigated. To investigate the rate of photo-degradation of CTC and TCH by the prepared catalysts, a quasi-level kinetic model was used to calculate the photocatalytic reaction rate constants by the $-\ln(C_t/C_0) = kt$ equation. The details are described in ESI Test S2.†

It was also found that there was little degradation effect of the g-C$_3$N$_4$/CoFe$_2$O$_4$/Bi$_2$MoO$_6$ composites on dyes, although their ability to degrade antibiotic-like substances was stronger. As shown in Fig. 11a, photodegradation experiments against

methyl orange (MO), methylene blue (MB), rhodamine B (RhB), and malachite green (MG) (20 mg L^{-1}) were carried out on the g-C$_3$N$_4$/CoFe$_2$O$_4$/Bi$_2$MoO$_6$ composites. The results showed that the g-C$_3$N$_4$/CoFe$_2$O$_4$/Bi$_2$MoO$_6$ composites mainly exhibited adsorption and desorption of the dyes, in which the adsorption and desorption processes of MB and MG were particularly pronounced, and was attributed to the presence of pore space and ionic adsorption. The ionic adsorption was particularly pronounced due to the magnetic nature of the composites.[46,47] In contrast, there was almost no removal of MO and RhB, which may be due to the mismatch between their molecules and the pores on the surface of the material.

The dyes were also mixed with carbon tetrachloride and TC to investigate the effect on the degradation rate of the composites in a system where the dyes and TC were simultaneously present.
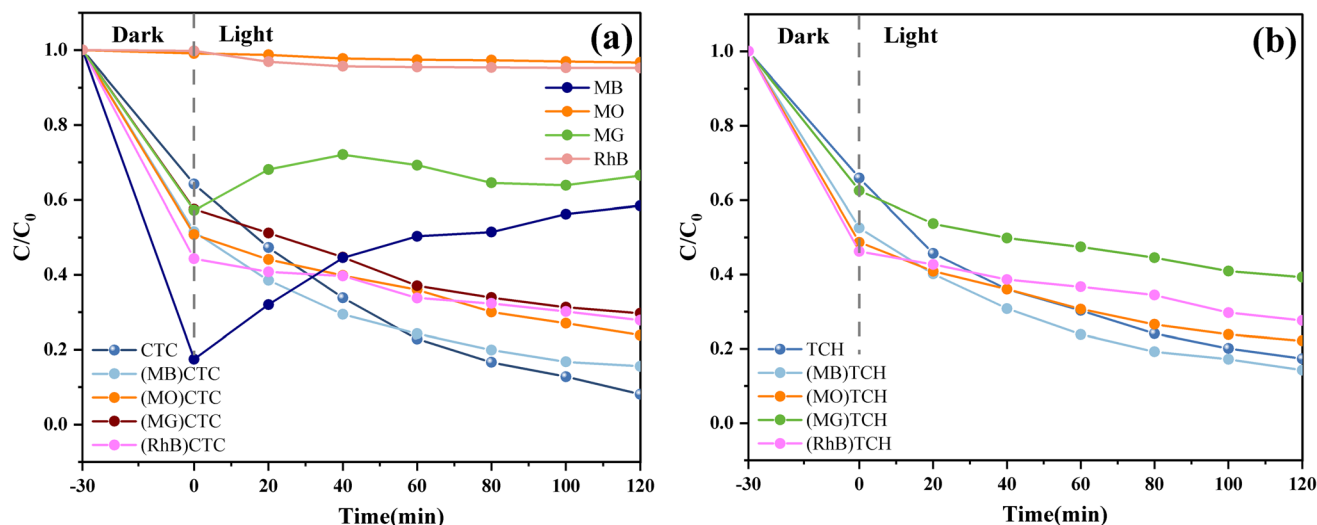

Fig. 11 Degradation curves of the mixture of dyes and antibiotics (CTC (a) and TCH (b)) under visible light irradiation with g-C$_3$N$_4$/CoFe$_2$O$_4$/Bi$_2$MoO$_6$ photocatalyst (photocatalyst) = 0.5 mg mL^{-1} (pollutant = 20 mg L^{-1}, 100 mL; Initial pH = 7; Temperature = 30 ± 0.5 °C).

The experimental results showed that the dyes negatively affected the degradation of both tetracyclines to varying degrees, and they reduced the degradation rate. However, the presence of MO increased the rate of TC degradation by the g-C_3N_4/$CoFe_2O_4$/Bi_2MoO_6 composites, which was attributed to the fact that the ionic adsorption of MO increased the adsorption of TC on the composites and improved the photocatalytic effect on the surface of the materials. The degradation curves of the hybrid system are shown in Fig. 11a and b.

Stability and rapid recovery are also considered to be important factors affecting catalytic performance in practical applications. Under the most optimal experimental conditions, 50 mg of g-C_3N_4/$CoFe_2O_4$/Bi_2MoO_6 photocatalyst was added, and its stability was tested through repeated degradation of 20 mg L^{-1} CTC solution. Therefore, the stability of the materials was investigated by studying the degradation of CTC and TCH by the CFB composite photocatalyst at four cycles of the experiment.

The results in Fig. 12 show that there was 90.0% and 80.3% degradation of CTC and TCH, respectively, by the magnetically recyclable CFB composite photocatalyst after 4 repeated cycles. The photocatalytic activity of the catalyst did not significantly change, indicating that the photocatalyst is stable and effective for the degradation of CTC and TCH. In particular, the cycling experiment resulted in a rapid separation of the material from the solution, which was made possible by the addition of the $CoFe_2O_4$ magnetic material and the applied magnetic field, thus providing the feasibility of the photocatalytic material to be used over a wide range of applications.

Fig. 12c shows that after four cycles of use, the magnetic saturation strength was 17.9 emu g^{-1} and did not significantly decrease before or after use. The composite continued to be magnetically separable, indicating the stable magnetic strength of the material. In addition, the SEM and XRD patterns of the g-C_3N_4/$CoFe_2O_4$/Bi_2MoO_6 samples before and after the recovery experiment were used to further verify the stability of the catalyst (Test S3†). The crystal phase composition of g-C_3N_4/$CoFe_2O_4$/Bi_2MoO_6 did not change, indicating that the structure of the photocatalyst did not change after the photocatalysis experiments. The above results indicate the
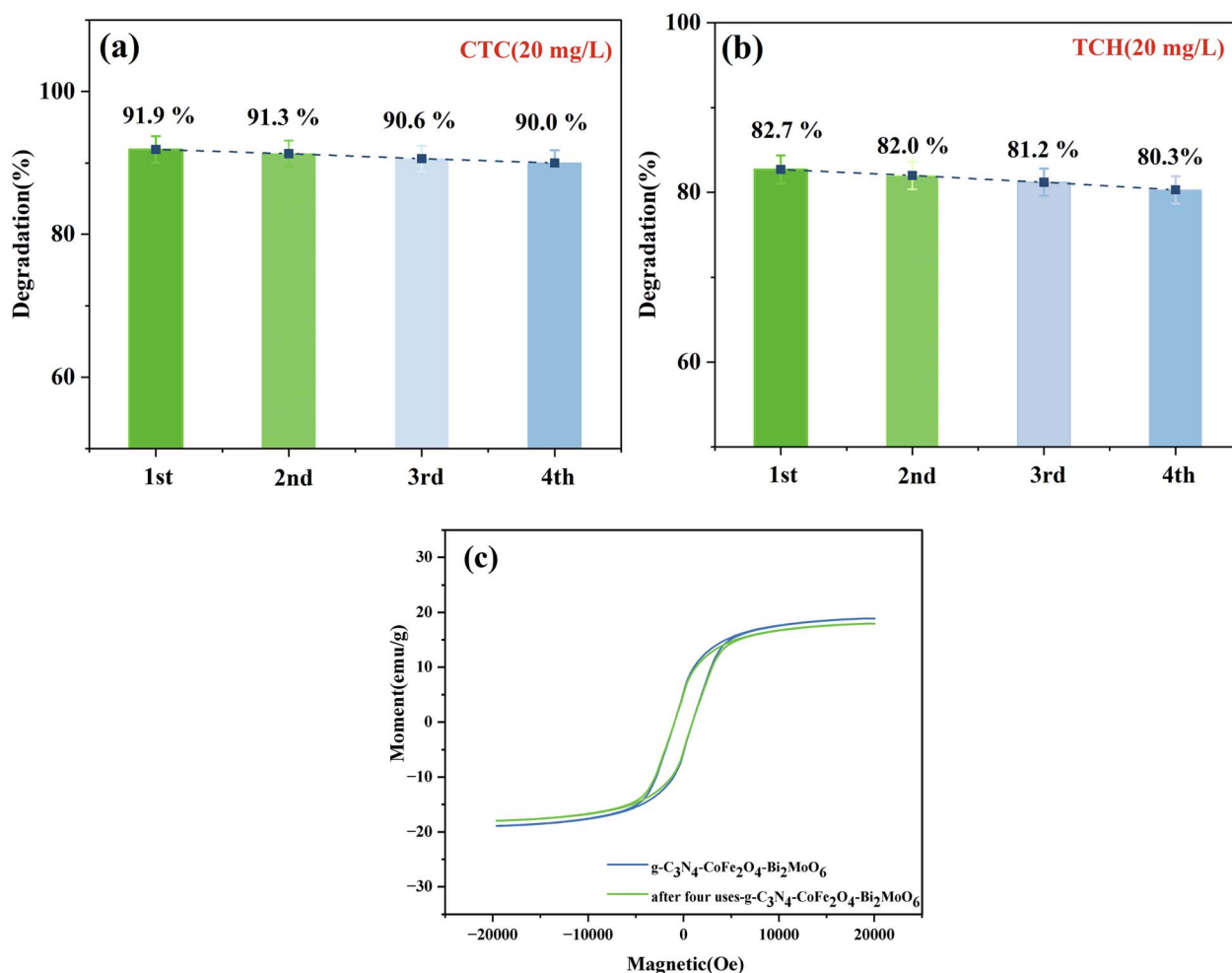

Fig. 12 (a and b) Recycling efficiency of the g-C_3N_4/$CoFe_2O_4$/Bi_2MoO_6 composites and (c) VSM spectrum of g-C_3N_4/$CoFe_2O_4$/Bi_2MoO_6 after four cycles of use.

excellent reusability and stability of g-C$_3$N$_4$/CoFe$_2$O$_4$/Bi$_2$MoO$_6$.

3.4 Photocatalytic degradation mechanism

To explore the photocatalytic degradation mechanism of the g-C$_3$N$_4$/CoFe$_2$O$_4$/Bi$_2$MoO$_6$ composite catalyst, a free radical capture experiment was used to study the active species of g-C$_3$N$_4$/CoFe$_2$O$_4$/Bi$_2$MoO$_6$ in the process of photocatalytic degradation of CTC. IPA, EDTA-2Na, and BQ are three sacrificial agents that are used to determine hydroxyl radical ($^\bullet$OH)

Fig. 13 Trapping of active species during the photocatalytic degradation of CTC over g-C$_3$N$_4$/CoFe$_2$O$_4$/Bi$_2$MoO$_6$ under visible light.

scavenger, hole (h$^+$) scavenger, and superoxide radical ($^\bullet$O$_2^-$) scavenger effects.

As shown in Fig. 13, after adding 1 mmol IPA, the photocatalytic degradation efficiency of CTC decreased from 91.9% to 52.4%, indicating that $^\bullet$OH is not a key active species in the photocatalytic process. After introducing 1 mmol EDTA-2Na and BQ, the photocatalytic degradation of CTC was significantly reduced, indicating that $^\bullet$O$_2^-$ and h$^+$ play a key role in the degradation of CTC. Based on the above data, the active species that play an important role in the photocatalytic system are $^\bullet$O$_2^-$ and h$^+$, and the role of $^\bullet$O$_2^-$ is particularly critical.

According to the calculation results for the previous M–S curve, the CB positions of g-C$_3$N$_4$ and Bi$_2$MoO$_6$ are −1.01 eV and −0.61 eV, respectively, which are all higher than −0.33 eV, indicating that photo-generated electrons can effectively dissolve oxygen molecules in water reduce to $^\bullet$O$_2^-$.

Ultimately, a possible ternary composite photocatalytic mechanism was proposed by combining the previously calculated band gap, the CB and VB positions of the pure components. The ternary heterojunction structure and the double Z-scheme appear in Fig. 14. In the conventional heterojunction structure, photogenerated electrons (e$^-$) are transferred from the CB of g-C$_3$N$_4$ and Bi$_2$MoO$_6$ to CoFe$_2$O$_4$ (0.41 eV). The photogenerated holes (h$^+$) of CoFe$_2$O$_4$ are transferred to the VB of g-C$_3$N$_4$ and Bi$_2$MoO$_6$. In contrast, CoFe$_2$O$_4$ is insufficient to reduce photogenerated electrons (e$^-$) to O$_2$ to $^\bullet$O$_2^-$. The standard oxidation potentials of g-C$_3$N$_4$ and Bi$_2$MoO$_6$ are greater than those of $^\bullet$OH/OH$^-$ (1.99 eV) and H$_2$O/$^\bullet$OH (2.68 eV), resulting in the inability of photogenerated holes (h$^+$) to oxidize OH$^-$ or H$_2$O to $^\bullet$OH.

Fig. 14 Mechanism of charge transfer and separation in the g-C$_3$N$_4$/CoFe$_2$O$_4$/Bi$_2$MoO$_6$ composite.

Fig. 15 Possible degradation path of TC in the g-C_3N_4/$CoFe_2O_4$/Bi_2MoO_6 composite photocatalyst.

Fig. 16 The toxicity prediction values and results for CTC and its intermediates calculated by TEST: (a) 96 hours fathead minnow LC50 and 48 hours *Daphnia magna* LC50, (b) bioaccumulation factor, developmental toxicity, and Ames mutagenicity test, and (c) oral rat LD50.

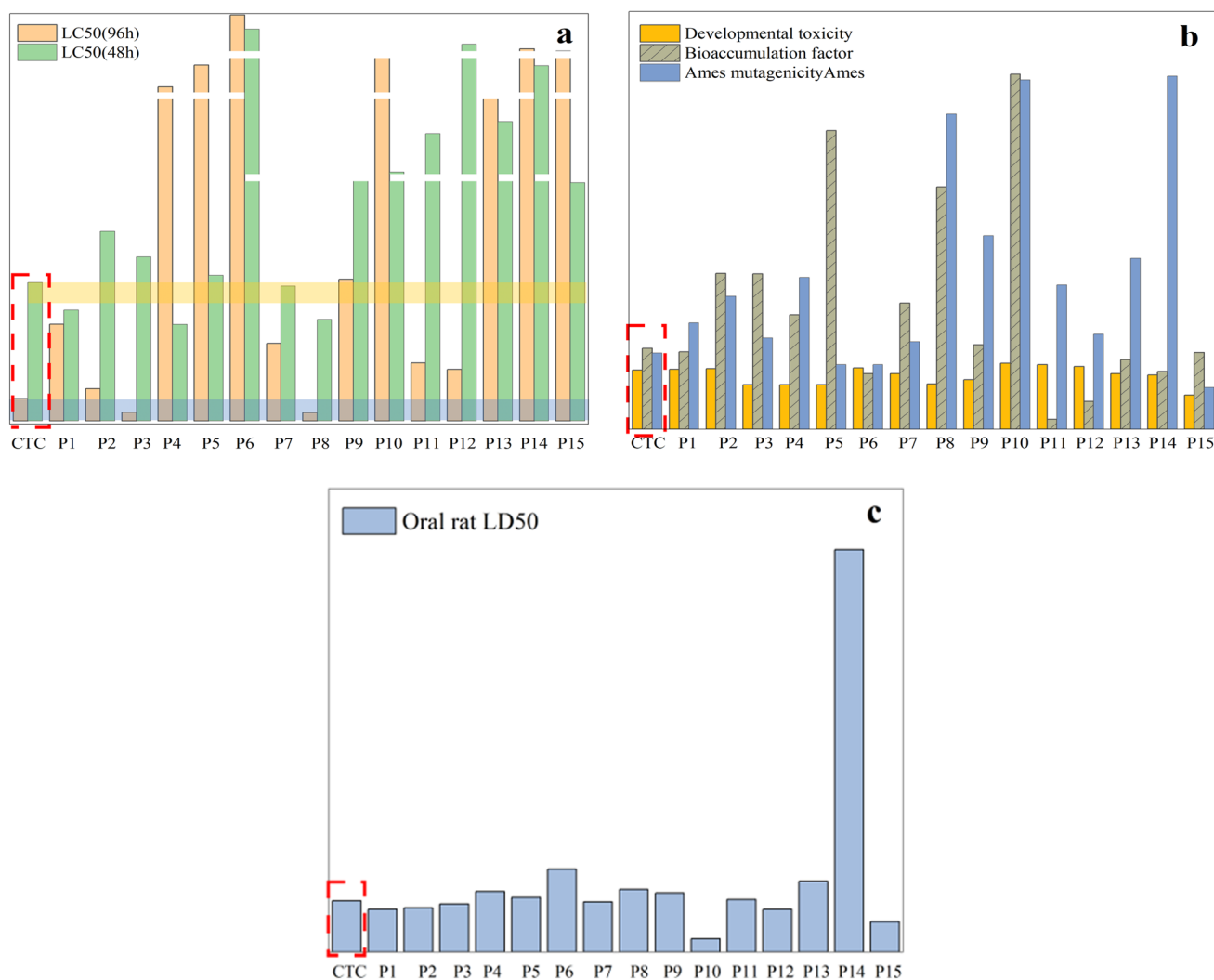The VB site of Bi_2MoO_6 can only consume OH^- to produce $\cdot OH$. However, $\cdot OH$ has little effect on the degradation of TC. Furthermore, in the ESR results above, g-C_3N_4/$CoFe_2O_4$/Bi_2MoO_6 produces $\cdot O_2^-$ and $\cdot OH$ under light irradiation, and therefore, the mechanism of the g-C_3N_4/$CoFe_2O_4$/Bi_2MoO_6 triplet complex is more in accordance with a double Z-scheme mechanism.[44] In this double Z-scheme structure, the photogenerated electrons located in the conduction band of $CoFe_2O_4$ are transferred to the VB of g-C_3N_4 and Bi_2MoO_6 so that the photogenerated electrons can reduce O_2 to produce $\cdot O_2^-$ for the oxidation of TC. The VB of Bi_2MoO_6 can only produce a small amount of surface hydroxyl groups and is far from being able to decompose water, and this mechanism is more reasonable considering that $\cdot O_2^-$ is the main substance used to degrade TC.

In this double Z-scheme structure, there are two transport channels for photogenerated electrons, facilitating the separation of photogenerated electron–hole pairs and the extension of the photogenerated carrier lifetime.[45] Additional superoxide radicals will be used to oxidize TC, and thus, the g-C_3N_4/$CoFe_2O_4$/Bi_2MoO_6 ternary composite photocatalyst exhibited excellent photocatalytic degradation performance.

3.5 Photocatalytic degradation pathway

GC-MS was used to study the degradation products of TC, and other intermediates were detected in the MS results, suggesting possible degradation pathways, as shown in Fig. 15. First, one molecule of H_2O was lost in the process from product ($m/z = 445$) to product P1 ($m/z = 427$). The intermediate product P2 ($m/z = 410$) is probably created by the relatively high electron density of the C–N bond, leading to the cleavage of C–NH$_2$. As additional rings open, other small molecule peaks appear ($m/z = 388, 320, 276,$ and 148).

In the second pathway, it is likely that P7 ($m/z = 386$) was produced by the deamination of the tetracycline molecule by the active substance and the oxygen molecule, forming a carbonyl group. Alternatively, we speculate that the material at P11 ($m/z = 414$) may have arisen after the initial oxidation. The mass spectral peak at P12 ($m/z = 399$) can be attributed to deamination and the formation of a ketone group at another position. The final products at P14 ($m/z = 206$) and P15 ($m/z = 136$) were obtained by ring opening of the material at P13 ($m/z = 340$).

3.6 Ecotoxicity test analysis

To determine whether the antibiotic CTC and its byproducts pose a threat to the ecosystem, the toxicity estimation software tool (TEST) was used to assess ecotoxicity. The specific experimental data have been described in ESI Tables S1 and S2.† Furthermore, the effective degradation of CTC is demonstrated more intuitively through plant growth experiments, and the ecotoxicity of the degradation system as a whole is low.

Fig. 16a shows that the LC50 (96 h) value of intermediates obtained with fathead fish was higher than that of CTC except for P3 and P8, among which the values of P6 and P14 were much higher than that of CTC. For P1, P4, P7, and P8, the LC50 (48 h) values of the intermediates obtained with *Daphnia magna* were higher than those of CTC, and the values of P6,

P10, P11, P12, P13, and P14 were much higher than those of CTC. This shows that the toxicity of CTC was significantly reduced after photodegradation. Fig. 16b shows that the developmental toxicity of intermediates was reduced to different degrees except for P1, P2, P6, P10, P11, and P12. As for mutagenicity, intermediates other than P8, P10, and P14 showed low mutagenicity, but the mutagenicity for P8, P9, P10, and P15 was negative.

It is worth noting that P8, P9, P10, and P14 are not harmful. In addition, the bioaccumulation factor of all intermediates was lower than that of CTC. For the oral LD50 of rats, there were higher LD50 values for other intermediates except for P1, P2, P3, P7, P10, P12, and P15, which indicated that some toxic intermediates will continue to be produced during photodegradation (Fig. 16c). Although some toxic intermediates remained, based on the above data, the overall biological toxicity was reduced. Further photocatalytic technology will be required to achieve overall non-toxicity of the CTC solution.

3.7 Plant growth test analysis

To further illustrate the effective degradation of antibiotics, plant cultures can be used to visualize the effect of antibiotic
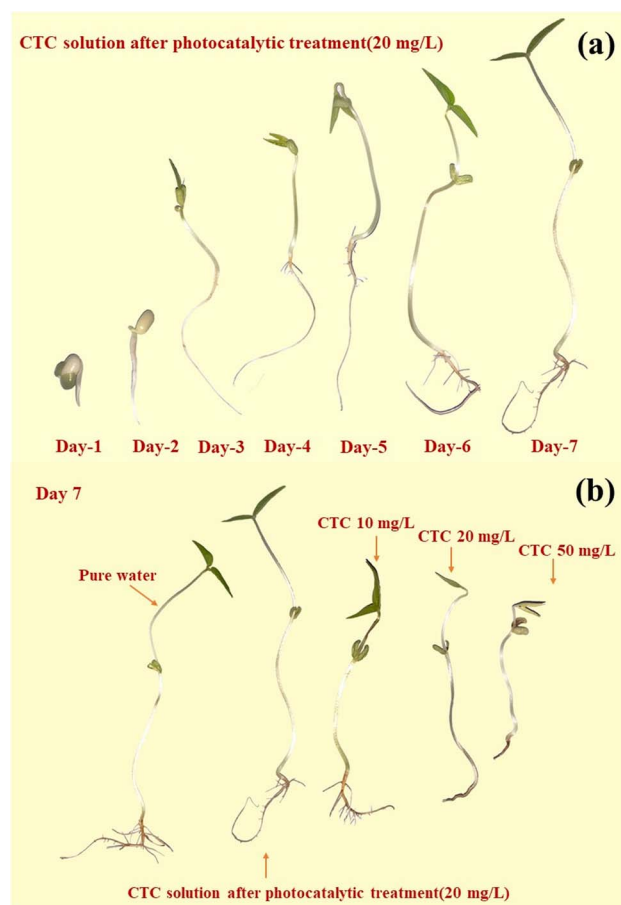

Fig. 17 Comparison of the growth process of mung beans under 20 mg L^{-1} CTC photocatalysis within 7 days (a) and the growth of mung beans under different conditions (b).

Table 1 Shoot growth of mung beans treated with pure water, photocatalytically treated solution of 20 mg L^{-1} CTC, and solutions of 10 mg L^{-1} CTC, 20 mg L^{-1} CTC, and 50 mg L^{-1} CTC

Treatment	Day 1	Day 2	Day 3	Day 4	Day 5	Day 6	Day 7
Pure water	1.0 ± 0.2	2.2 ± 0.4	5.8 ± 0.4	8.7 ± 0.5	10.5 ± 0.5	13.5 ± 0.6	15.5 ± 0.6
CTC (20 mg L^{-1}) solution after degradation	0.9 ± 0.5	2.1 ± 0.5	3.5 ± 0.5	8.0 ± 0.6	10.5 ± 0.5	13.4 ± 0.8	15.5 ± 0.7
CTC 10	1.0 ± 0.1	2.0 ± 0.3	3.7 ± 0.3	5.0 ± 0.4	8.3 ± 0.5	10.6 ± 0.5	11.0 ± 0.6
CTC 20	0.8 ± 0.1	1.9 ± 0.2	2.3 ± 0.3	4.7 ± 0.3	6.0 ± 0.3	7.3 ± 0.4	9.5 ± 0.5
CTC 50	0.7 ± 0.1	1.3 ± 0.2	1.5 ± 0.2	4.4 ± 0.4	5.7 ± 0.4	7.0 ± 0.6	8.2 ± 0.6

content on the growth of plants by observing the morphology of their growth. In this study, mung bean seeds, which are easy to grow, were selected for culture. Under normal conditions, none of the various concentrations of antibiotics we used would significantly affect the germination rate of mung bean seeds. However, the concentration of the antibiotics significantly affected the growth process, with the growth of the mung bean seeds slowing as the concentration of the antibiotics increased.

By observing the growth cycle of the plants, it is clear that high concentrations of antibiotics affected the growth of the plant rhizomes, causing browning and molding of the rhizomes. This is particularly true for the growth of the plant's root whiskers, as at antibiotic concentrations of 20 mg L^{-1} and 50 mg L^{-1}, the plants are essentially rootless. Fig. 17 shows the growth of mung bean seeds after photocatalytic treatment in pure water and in a solution of 20 mg L^{-1} CTC, and solutions of 10 mg L^{-1} CTC, 20 mg L^{-1} CTC, and 50 mg L^{-1} CTC for 7 days. Also, Table 1 shows the shoot growth of mung bean seeds for 7 days under different concentrations of treatment.

On day three, the mung bean seeds treated with 20 mg L^{-1} CTC solution and 50 mg L^{-1} CTC solution showed significant retardation of growth compared to the other concentration treatments. On the fourth day, mung bean seeds treated with 10 mg L^{-1} CTC solution also showed retarded growth compared to mung bean seeds cultivated with pure water and photocatalytically treated 20 mg L^{-1} CTC solution. Not only was the shoot length insufficient, but there was also no root whisker growth.

After a growth cycle of 7 days, there was little difference in the growth of mung bean seeds cultivated with pure water and mung bean seeds cultivated with photocatalytically treated 20 mg L^{-1} CTC solution, but the overall growth of mung bean seeds cultivated with pure water was more optimal with a greater amount of root whiskers. The 10 mg L^{-1} group also showed root whisker growth, while there was no root whisker growth for the 20 mg L^{-1} and 50 mg L^{-1} groups. Thus, this simple plant growth experiment showed that the antibiotics in the solution were effectively degraded by the photocatalytic treatment, and low ecotoxicity of degradation products was present.

4   Conclusion

A novel magnetically recyclable g-C$_3$N$_4$/CoFe$_2$O$_4$/Bi$_2$MoO$_6$ photocatalyst was synthesized by a simple solvothermal method, and it exhibited excellent photocatalytic performance in

degrading antibiotics and was easy to recycle. On the one hand, the internal electric field present in the double Z-type heterojunction can accelerate the separation and migration of photogenerated carriers. On the other hand, the specific surface area of the composite was significantly larger than that of the Bi$_2$MoO$_6$ monomer, which provides abundant reaction sites for photocatalysis. In addition, there was an overall reduction of the toxicity of its degradation intermediates and degradation solutions compared to that of gentamicin and tetracycline. This study provides a new idea for the removal of organic pollutants using light energy.

Author contributions

Zhiwei Tang: conceptualization, methodology, writing – original draft preparation, software. Changchao Hu: conceptualization, methodology, validation, writing – review and editing. Rui Zhang: data curation, validation, writing – review and editing. Junrong Yu, Lu Cai, Ze Yang, Xingwang Wang, Shiqiang Wu, Desheng Liu: software, formal analysis, visualization.

Conflicts of interest

There are no conflicts of interest to declare.

Acknowledgements

References

1 Z. Wei, J. Liu and W. Shangguan, A review on photocatalysis in antibiotic wastewater: Pollutant degradation and hydrogen production, *Chin. J. Catal.*, 2020, **41**, 1440–1450, DOI: **10.1016/S1872-2067(19)63448-0**.

2 H. Shi, Degradation of tetracyclines in manure-amended soil and their uptake by litchi (Litchi chinensis Sonn.), *Environ. Sci. Pollut. Res.*, 2019, **26**, 6209–6215, DOI: **10.1007/s11356-018-04077-y**.

3 A. Ghirardini, V. Grillini and P. Verlicchi, A review of the occurrence of selected micropollutants and microorganisms in different raw and treated manure -

Environmental risk due to antibiotics after application to soil, *Sci. Total Environ.*, 2020, **707**, 27, DOI: **10.1016/j.scitotenv.2019.136118**.

4 I. Chopra and M. Roberts, Tetracycline antibiotics: mode of action, applications, molecular biology, and epidemiology of bacterial resistance, *Microbiol. Mol. Biol. Rev.*, 2001, **65**, 232–260, DOI: **10.1128/MMBR.65.2.232-260.2001**.

5 S. L. Wang and H. Wang, Adsorption behavior of antibiotic in soil environment: a critical review, *Front. Environ. Sci. Eng.*, 2015, **9**, 565–574, DOI: **10.1007/s11783-015-0801-2**.

6 S. Shurbaji, P. T. Huong and T. M. Altahtamouni, Review on the Visible Light Photocatalysis for the Decomposition of Ciprofloxacin, Norfloxacin, Tetracyclines, and Sulfonamides Antibiotics in Wastewater, *Catalysts*, 2021, **11**, 26–29, DOI: **10.3390/catal11040437**.

7 F. Guo, *et al.*, Construction of Cu_3P-$ZnSnO_3$-g-C_3N_4 p-n-n heterojunction with multiple built-in electric fields for effectively boosting visible-light photocatalytic degradation of broad-spectrum antibiotics, *Sep. Purif. Technol.*, 2021, **265**, 11, DOI: **10.1016/j.seppur.2021.118477**.

8 H. Y. Niu and Y. Q. Cai, Preparation of Octadecyl and Amino Mixed Group Modified Titanate Nanotubes and Its Efficient Adsorption to Several Ionic or Ionizable Organic Analytes, *Anal. Chem.*, 2009, **81**, 9913–9920, DOI: **10.1021/ac901531k**.

9 S. H. Wang, H. Y. Niu, D. Cao and Y. Q. Cai, Covalent-organic frameworks as adsorbent and matrix of SALDI-TOF MS for the enrichment and rapid determination of fluorochemicals, *Talanta*, 2019, **194**, 522–527, DOI: **10.1016/j.talanta.2018.10.071**.

10 K. Stoob, H. P. Singer, S. R. Mueller, R. P. Schwarzenbach and C. H. Stamm, Dissipation and transport of veterinary sulfonamide antibiotics after manure application to grassland in a small catchment, *Environ. Sci. Technol.*, 2007, **41**, 7349–7355, DOI: **10.1021/es070840e**.

11 M. O. Aust, Distribution of sulfamethazine, chlortetracycline and tylosin in manure and soil of Canadian feedlots after subtherapeutic use in cattle, *Environ. Pollut.*, 2008, **156**, 1243–1251, DOI: **10.1016/j.envpol.2008.03.011**.

12 M. Forster, Sequestration of Manure-Applied Sulfadiazine Residues in Soils, *Environ. Sci. Technol.*, 2009, **43**, 1824–1830, DOI: **10.1021/es8026538**.

13 R. Daghrir and P. Drogui, Tetracycline antibiotics in the environment: a review, *Environ. Chem. Lett.*, 2013, **11**, 209–227, DOI: **10.1007/s10311-013-0404-8**.

14 R. R. Kumar, J. T. Lee and J. Y. Cho, Fate, Occurrence, and Toxicity of Veterinary Antibiotics in Environment, *J. Korean Soc. Appl. Biol. Chem.*, 2012, **55**, 701–709, DOI: **10.1007/s13765-012-2220-4**.

15 E. Patyra, E. Kowalczyk, A. Grelik, M. Przenioslo-Siwczynska and K. Kwiatek, Screening method for the determination of tetracyclines and fluoroquinolones in animal drinking water by liquid chromatography with diode array detector, *Pol. J. Vet. Sci.*, 2015, **18**, 283–289, DOI: **10.1515/pjvs-2015-0037**.

16 M. Pan, C. K. C. Wong and L. M. Chu, Distribution of Antibiotics in Wastewater-Irrigated Soils and Their Accumulation in Vegetable Crops in the Pearl River Delta, Southern China, *J. Agric. Food Chem.*, 2014, **62**, 11062–11069, DOI: **10.1021/jf503850v**.

17 B. J. A. Berendsen, The persistence of a broad range of antibiotics during calve, pig and broiler manure storage, *Chemosphere*, 2018, **204**, 267–276, DOI: **10.1016/j.chemosphere.2018.04.042**.

18 P. Wang, C. Xu, X. Zhang, Q. Yuan and S. Shan, Effect of photocatalysis on the physicochemical properties of liquid digestate, *Environ. Res.*, 2023, **223**, 115467, DOI: **10.1016/j.envres.2023.115467**.

19 Y. Z. Hong, Rational design 2D/3D MoS_2/In_2O_3 composites for great boosting photocatalytic H_2 production coupled with dye degradation, *J. Taiwan Inst. Chem. Eng.*, 2023, **146**, 11, DOI: **10.1016/j.jtice.2023.104862**.

20 Y. Tian, Facile template-free fabrication of different micro/nanostructured In_2O_3 for photocatalytic H_2 production from glucose solution, *Int. J. Hydrogen Energy*, 2024, **51**, 475–487, DOI: **10.1016/j.ijhydene.2023.08.223**.

21 Y. Shimodaira, H. Kato, H. Kobayashi and A. Kudo, Photophysical properties and photocatalytic activities of bismuth molybdates under visible light irradiation, *J. Phys. Chem. B*, 2006, **110**, 17790–17797, DOI: **10.1021/jp0622482**.

22 T. O. Ajiboye, O. A. Oyewo and D. C. Onwudiwe, The performance of bismuth-based compounds in photocatalytic applications, *Surf. Interfaces*, 2021, **23**, 100927, DOI: **10.1016/j.surfin.2021.100927**.

23 H. H. Li, K. W. Li and H. Wang, Hydrothermal synthesis and photocatalytic properties of bismuth molybdate materials, *Mater. Chem. Phys.*, 2009, **116**, 134–142, DOI: **10.1016/j.matchemphys.2009.02.058**.

24 Y. S. Xu and W. D. Zhang, Monodispersed Ag_3PO_4 nanocrystals loaded on the surface of spherical Bi_2MoO_6 with enhanced photocatalytic performance, *Dalton Trans.*, 2013, **42**, 1094–1101, DOI: **10.1039/c2dt31634j**.

25 A. Kumar, Construction of dual Z-scheme g-C_3N_4/$Bi^4Ti^3O^{12}$/$Bi^4O^5I^2$ heterojunction for visible and solar powered coupled photocatalytic antibiotic degradation and hydrogen production: Boosting via I^-/I^{3-} and Bi^{3+}/Bi^{5+} redox mediators, *Appl. Catal., B*, 2021, **284**, 119808, DOI: **10.1016/j.apcatb.2020.119808**.

26 X. Q. Fan, Constructing carbon-nitride-based copolymers via Schiff base chemistry for visible-light photocatalytic hydrogen evolution, *Appl. Catal., B*, 2016, **182**, 68–73, DOI: **10.1016/j.apcatb.2015.09.006**.

27 E. Liu, Rational copolymerization strategy engineered C self-doped g-C_3N_4 for efficient and robust solar photocatalytic H_2 evolution, *Renewable Energy*, 2021, **178**, 757–765, DOI: **10.1016/j.renene.2021.06.066**.

28 F. Guo, Cu_3P nanoparticles decorated hollow tubular carbon nitride as a superior photocatalyst for photodegradation of tetracycline under visible light, *Sep. Purif. Technol.*, 2021, **275**, 10, DOI: **10.1016/j.seppur.2021.119223**.

29 H. Yuan, Dual-channels separated mechanism of photo-generated charges over semiconductor photocatalyst for hydrogen evolution: Interfacial charge transfer and transport dynamics insight, *Chem. Eng. J.*, 2023, **454**, 12, DOI: **10.1016/j.cej.2022.140442**.

30 S. W. Cao, J. X. Low, J. G. Yu and M. Jaroniec, Polymeric Photocatalysts Based on Graphitic Carbon Nitride, *Adv. Mater.*, 2015, **27**, 2150–2176, DOI: 10.1002/adma.201500033.

31 F. F. Liang and Y. F. Zhu, Enhancement of mineralization ability for phenol via synergetic effect of photoelectrocatalysis of g-C$_3$N$_4$ film, *Appl. Catal., B*, 2016, **180**, 324–329, DOI: 10.1016/j.apcatb.2015.05.009.

32 M. W. Kadi, R. M. Mohamed, A. A. Ismail and D. W. Bahnemann, Decoration of g-C$_3$N$_4$ nanosheets by mesoporous CoFe$_2$O$_4$ nanoparticles for promoting visible-light photocatalytic Hg(II) reduction, *Colloids Surf., A*, 2020, **603**, 10–15, DOI: 10.1016/j.colsurfa.2020.125206.

33 B. G. Wang and B. Zhao, Carbon Dots/CoFe$_2$O$_4$ Mesoporous Nanosphere Composites As a Magnetically Separable Visible Light Photocatalyst, *Russ. J. Phys. Chem. A*, 2019, **93**, 393–399, DOI: 10.1134/S0036024419020043.

34 E. Ferdosi, H. Bahiraei and D. Ghanbari, Investigation the photocatalytic activity of CoFe$_2$O$_4$/ZnO and CoFe$_2$O$_4$/ZnO/Ag nanocomposites for purification of dye pollutants, *Sep. Purif. Technol.*, 2019, **211**, 35–39, DOI: 10.1016/j.seppur.2018.09.054.

35 R. Tabit, Magnetic CoFe$_2$O$_4$ nanoparticles supported on graphene oxide (CoFe$_2$O$_4$/GO) with high catalytic activity for peroxymonosulfate activation and degradation of rhodamine B, *RSC Adv.*, 2018, **8**, 1351–1360, DOI: 10.1039/c7ra09949e.

36 K. Kumar, S. C. Gupta, S. K. Baidoo, Y. Chander and C. J. Rosen, Antibiotic uptake by plants from soil fertilized with animal manure, *J. Environ. Qual.*, 2005, **34**, 2082–2085, DOI: 10.2134/jeq2005.0026.

37 M. H. Farkas, J. O. Berry and D. S. Aga, Chlortetracycline Detoxification in Maize via Induction of Glutathione S-Transferases after Antibiotic Exposure, *Environ. Sci. Technol.*, 2007, **41**, 1450–1456, DOI: 10.1021/es061651j.

38 Y. Lv, Effective degradation of norfloxacin on Ag$_3$PO$_4$/CNTs photoanode: Z-scheme mechanism, reaction pathway, and toxicity assessment, *Chem. Eng. J.*, 2022, **429**, 132092, DOI: 10.1016/j.cej.2021.132092.

39 Y. J. Wang, X. J. Bai, C. S. Pan, J. He and Y. F. Zhu, Enhancement of photocatalytic activity of Bi$_2$WO$_6$ hybridized with graphite-like C3N4, *J. Mater. Chem.*, 2012, **22**, 11568–11573, DOI: 10.1039/c2jm16873a.

40 P. F. Xia, B. C. Zhu, J. G. Yu, S. W. Cao and M. Jaroniec, Ultra-thin nanosheet assemblies of graphitic carbon nitride for enhanced photocatalytic CO$_2$ reduction, *J. Mater. Chem. A*, 2017, **5**, 3230–3238, DOI: 10.1039/c6ta08310b.

41 J. G. Yu, S. H. Wang, B. Cheng, Z. Lin and F. Huang, Noble metal-free Ni(OH)$_{(2)}$-g-C$_3$N$_4$ composite photocatalyst with enhanced visible-light photocatalytic H-2-production activity, *Catal. Sci. Technol.*, 2013, **3**, 1782–1789, DOI: 10.1039/c3cy20878h.

42 R. Wang, Mechanism insight into rapid photocatalytic disinfection of Salmonella based on vanadate QDs-interspersed g-C$_3$N$_4$ heterostructures, *Appl. Catal., B*, 2018, **225**, 228–237, DOI: 10.1016/j.apcatb.2017.11.060.

43 W. Liu, J. Shen, X. F. Yang, Q. Q. Liu and H. Tang, Dual Z-scheme g-C$_3$N$_4$/Ag$_3$PO$_4$/Ag$_2$MoO$_4$ ternary composite photocatalyst for solar oxygen evolution from water splitting, *Appl. Surf. Sci.*, 2018, **456**, 369–378, DOI: 10.1016/j.apsusc.2018.06.156.

44 Q. L. Xu, Direct Z-scheme photocatalysts: Principles, synthesis, and applications, *Mater. Today*, 2018, **21**, 1042–1063, DOI: 10.1016/j.mattod.2018.04.008.

45 W. K. Jo and T. S. Natarajan, Fabrication and efficient visible light photocatalytic properties of novel zinc indium sulfide (ZnIn$_2$S$_4$) - graphitic carbon nitride (g-C$_3$N$_4$)/bismuth vanadate (BiVO$_4$) nanorod-based ternary nanocomposites with enhanced charge separation via Z-scheme transfer, *J. Colloid Interface Sci.*, 2016, **482**, 58–72, DOI: 10.1016/j.jcis.2016.07.062.

46 L. L. Hu, M. Li, L. H. Cheng, B. F. Jiang and J. P. Ai, Solvothermal synthesis of octahedral and magnetic CoFe$_2$O$_4$-reduced graphene oxide hybrids and their photo-Fenton-like behavior under visible-light irradiation, *RSC Adv.*, 2021, **11**, 22250–22263, DOI: 10.1039/d1ra03103a.

47 Y. Shi, Ternary graphene–CoFe$_2$O$_4$/CdS nanohybrids: preparation and application as recyclable photocatalysts, *J. Mater. Chem. A*, 2014, **2**, 535–544, DOI: 10.1039/C3TA13409A.